Nanoscale Origin of Strong Charge Carrier Scattering at Grain Boundaries in Orthorhombic SnSe Semiconductor Thin Films

Xinyi He[1,2], *Kenji Matsuo*[1], *Takayoshi Katase*[1,3,*], *Kota Hanzawa*[3], *Hideto Yoshida*[4], *Shigenori Ueda*[5,6], *Hidenori Hiramatsu*[1,3], *Hideo Hosono*[1],*and Toshio Kamiya*[1,3,*]

[1] MDX Research Center for Element Strategy, Institute of Integrated Research, Institute of Science Tokyo, 4259 Nagatsuta, Midori, Yokohama 226-8501, Japan

[2] Kanagawa Institute of Industrial Science and Technology, 705-1 Shimoimaizumi, Ebina, Kanagawa 243-0435, Japan

[3] Materials and Structures Laboratory, Institute of Integrated Research, Institute of Science Tokyo, 4259 Nagatsuta, Midori, Yokohama, 226-8501, Japan

[4] SANKEN, Osaka University, 8-1 Mihogaoka, Ibaraki, Osaka 567-0047, Japan

[5] Research Center for Electronic and Optical Materials, National Institute for Materials Science (NIMS), 1-1 Namiki, Tsukuba, Ibaraki, 305-0044, Japan

[6]Synchrotron X-ray Station at SPring-8, NIMS, 1-1 Sayo, Hyogo 679-5148, Japan

* Correspondence to: katase.t.aa@m.titech.ac.jp, kamiya.t.aa@m.titech.ac.jp

Keywords: Tin selenide; Thermoelectric material; Epitaxial film; Carrier transport; Defect; Density functional theory

ABSTRACT: Tin mono-selenide (SnSe) is one of the high-performance thermoelectric materials, and recent progress has been made in its application to thin-film thermoelectric devices. However, the performance of SnSe polycrystalline and epitaxial films has been limited by their electronic conductivity lower than the single crystal due to strong carrier scattering. In this paper, we investigated the origin of carrier scattering through nanoscale characterization of *a*-axis oriented SnSe films with different grain boundary (GB) structures (i.e., *a*-axis misorientations and in-plane rotational GBs). The *a*-axis oriented SnSe polycrystalline films grown on glass substrates and epitaxial films on MgO (001) substrates show p-type conduction. In-grain carrier mobility increases with the increased grain size and improved out-of-plane *a*-axis orientation at higher growth temperatures, but the hole transport in the films is dominated by GB scattering. For SnSe films with the out-of-plane misorientation angles larger than 5°, GBs form potential barriers with a height (E_b) of up to 62 meV and significantly reduce carrier mobility (μ). Meanwhile, when the out-of-plane misorientation angles are less than 5°, the effect of *a*-axis orientation fluctuations on μ becomes small, but the room-temperature μ is limited to ~50 cm^2/(Vs), regardless of the different in-plane misorientations. It is found that (100) SnSe epitaxial films on a MgO (001) substrate form 90° rotational domains composed of in-plane [011] and [01-1] oriented grains, and have GB potential barriers with E_b = 30 meV, which is lower than those in the *a*-axis misoriented SnSe polycrystalline films but still deteriorates μ. Density functional theory calculations show that the 90° rotational domain boundary causes a shift of SnSe molecular layers between the [011] and [01-1] oriented grains, and the distorted Sn−Se_3 polyhedra form hole trap states above the fundamental valence band maximum, which can explain the formation of the GB potential barriers. Controlling crystallite orientation and size is a critical factor to realize high μ SnSe films for thermoelectric device applications.

1. INTRODUCTION

Tin mono-selenide (SnSe) has received great attention as a high-performance thermoelectric material with a record conversion efficiency (*ZT*) of up to 2.6 for single crystals.[1] SnSe is a p-type semiconductor with a band gap of 0.9–1.0 eV,[2,3] and its single crystals exhibit a high hole mobility (μ) of ~200 cm^2/(Vs) at room temperature (RT).[4-7] On the other hand, we previously reported high-quality SnSe epitaxial films on MgO (001) substrates.[8] The SnSe epitaxial film exhibits μ ~50 cm^2/(Vs) with a low hole concentration ~8×10^{15} cm^{-3} at RT. Additionally, a high μ ~50 cm^2/(Vs) in maximum was demonstrated also for SnSe polycrystalline films on glass substrates, and a relatively high μ ~10 cm^2/(Vs) was achieved in SnSe films deposited even at RT (without heating the substrate). Therefore, SnSe is a promising semiconductor for thin film devices that can be formed at low temperatures on glass or flexible substrates. Recently, significant progress has been made in thin film growth,[9,10] carrier doping,[11-12] investigation of thermoelectric properties,[13-17] and development of thin-film thermoelectric modules.[12,18] However, the electrical conductivity of SnSe polycrystalline and epitaxial films has been an order of magnitude lower than that of single crystal, because the μ of polycrystalline/epitaxial films are limited by strong carrier scattering.

SnSe has a GeS-type orthorhombic crystal structure (space group: *Pnma*) composed of alternately stacked one-molecule-thick SnSe layers along the *a*-axis (**Fig. 1**).[19] Each SnSe layer has Sn–Se_3 coordination structure (purple polyhedron), in which an Sn atom is coordinated by two Se atoms in the same *b*–*c* plane and one Se atom at the adjacent atomic plane in the stacking direction. The layered structure of SnSe causes highly anisotropic carrier transport; i.e., the effective masses of holes along the *a*-axis (perpendicular to the layer) are much larger than those along the *b*- and *c*-axes (parallel to the layer),[20] indicating that much higher μ can be realized along the in-plane *b*- and *c*-axes rather than those along the out-of-plane *a*-axis. In addition, SnSe exhibits strong in-plane anisotropy in electrical conductivity,[21]

due to the different atomic structures and bonding characteristics along the *b*- and *c*-axes (**Fig. 1**). Rock-salt type atomic arrangement is seen along the *b*-axis (left panel of **Fig. 1**), while the adjacent SnSe layer is shifted by [0, 0, 0.38] in fractional coordinates along the *c*-axis, as indicated by the arrow in right panel of **Fig. 1**. The *a*-axis oriented SnSe films can be grown on MgO (001) and glass substrates, which is advantageous for achieving high μ films. However, the orthorhombic lattice of SnSe along the *b*- and *c*-axes forms in-plane 90° rotational domain structures in the *a*-axis oriented epitaxial films on MgO (001) substrates, which likely cause strong carrier scattering and reduces μ to ~50 $cm^2/(Vs)$, which is far lower than that of single crystal ~200 $cm^2/(Vs)$.[8] On the other hand, the μ of *a*-axis oriented SnSe polycrystalline films on glass substrates was expected to further decrease compared to the epitaxial films. Interestingly, nearly the same $\mu \sim$ 50 $cm^2/(Vs)$ is maintained despite the completely unoriented domains along the in-plane direction. The electronic performance of polycrystalline thin films critically depends on the crystallite quality of each domain and the properties of grain boundaries (GBs). Typically, strain, defects, and dislocations formed at GBs act as strong scattering centers for carrier transport.[22] Also, charge trapping states formed at the GBs create potential barriers for carrier transport, limiting the μ. The broken local symmetry and chemical bonding strongly affect the electronic states at GBs.[23] Understanding the effects of crystallite misorientations and rotational GBs on carrier transport of layered SnSe thin films is crucial to design and improve semiconductor devices.

In this paper, we investigate the electron transport properties of *a*-axis oriented SnSe films with different GB structures such as *a*-axis misorientations and rotational GBs, and evaluate the electronic structure of 90° rotational GBs to explore the nanoscale origin of strong carrier scattering. SnSe polycrystalline and epitaxial films grown on glass and MgO (001) substrates exhibit p-type conduction, and the hole transport in the films is dominated by GB scattering at RT. We evaluate GB characteristics from temperature dependence of μ, and discuss the correlation between carrier transport and microstructures of the SnSe films.

2. EXPERIMENTAL SECTION

2.1. Thin film growth. 100-nm thick SnSe films were fabricated on alkali-free glass substrates (Corning® EAGLE XG®) at growth temperature (T_g) = RT−500 °C in a vacuum by pulsed laser deposition (PLD). A SnSe epitaxial film was grown on a MgO (001) substrate at T_g = 500 °C. Note that the maximum T_g was limited by severe re-evaporation of the films at ≥ 600 °C. The Se-rich $SnSe_{1.2}$ bulk polycrystal was used as a PLD target, because the transferability of Se from the PLD target to thin films is lower than that of Sn even at low temperatures.[8,24,25] A KrF excimer laser (wavelength of 248 nm) with a repetition rate of 10 Hz was used to ablate the $SnSe_{1.2}$ polycrystalline target. The base pressure of deposition chamber was ~1×10^{-5} Pa. Note that we first optimized the growth rate for SnSe films on glass substrates at T_g = 500 °C by changing laser energy fluence from 0.6 to 3 J/cm^2 (**Fig. S1** of Supporting Information). Lower growth rate increased the μ, and the decrease of nucleation density led to increase of grain sizes and the improved crystallite orientation. Therefore, the film growth rate was optimized at the lowest value of 0.4 nm/s.

2.2. Thin film characterization. Lattice parameters and crystal orientation of SnSe films for out-of-plane (i.e., perpendicular to the sample surface) and in-plane (i.e., parallel to the surface) were analyzed by x-ray diffraction (XRD) using a Smart Lab. (Rigaku Corp.). The films on glass substrates were measured by XRD with a parallel-beam Cu Kα radiation source at RT. The films on the MgO (001) substrate were measured by high-resolution XRD with a parallel-beam Cu $K\alpha_1$ radiation source monochromated with a two-bounce Ge (220) crystal. The out-of-plane measurements were performed by ω-coupled 2θ scans, while the in-plane measurements were performed by ϕ-coupled $2\theta_\chi$ scans. For in-plane measurements, the x-ray incident angle was set to the total reflection critical angle, ω ~0.5°. For the SnSe films on MgO substrate, $2\theta_\chi$ was initially set at 200 diffraction angle of MgO and ϕ was adjusted to the

strongest peak position, after which ϕ-coupled $2\theta_\chi$ scans were performed. In-plane crystallite sizes (D) were estimated from Scherrer's equation of $D = K\lambda/(\beta\cos\theta)$, where K is the Scherrer constant ($K = 0.94$), λ the wavelength of x-ray, β the full width at half-maximum (FWHM) value of diffraction peak, and θ the Bragg angle. The β values were obtained from 020 diffraction peaks for the SnSe films on glass substrates and 002 diffraction peak for the SnSe film on the MgO substrate by in-plane XRD. The intrinsic β values of the samples were estimated by correcting the apparatus function using the Gaussian profile approximation, $\beta_{\mathrm{intrinsic}} = \sqrt{(\beta_{\mathrm{SnSe}})^2 - (\beta_{\mathrm{MgO}})^2}$ (β_{MgO} is a FWHM from a reference 'ideal' sample. We employed the 200 diffraction peak of the MgO single crystal). Since the obtained β values are dependent on θ, it is preferable to use the diffraction peaks (200 or 020) of SnSe, whose diffraction angles are close to those of the 200 diffraction peak of MgO. The tilting angle of the crystallites was analyzed by 2θ-fixed ω scans (out-of-plane x-ray rocking curve). The in-plane orientation of the crystallites was investigated by $2\theta_\chi$-fixed ϕ scans (in-plane x-ray rocking curve). The film thickness (d) was determined by x-ray reflectivity measurement. The chemical composition (i.e., atomic ratio of Sn and Se) was evaluated with an electron probe micro analyzer (EPMA). Film surface morphology was observed by atomic force microscopy (AFM). Microstructure observation of the films was conducted by a scanning transmission electron microscope (STEM, JEM-ARM200F, JEOL Ltd.) with an acceleration voltage of 200 kV, where the samples were thinned by focused ion beam (FIB) and Ar^+ ion milling.

Electronic properties from RT to lower temperatures were measured by the Hall effect using the van der Pauw configuration under AC-modulated magnetic fields of 0.35 T (ResiTest 8300, Toyo Corp.), which provided electrical conductivity (σ), Hall coefficient (R_{H}), carrier concentration (n), and μ. Constant current of 1 μA was applied for the Hall effect measurements. Pt electrode, deposited by electron-beam evaporation, was used for Ohmic contact.

2.3. Density functional theory calculation. Electronic structure calculations of SnSe model

with rotational GBs (explained later in detail) were conducted using the projector-augmented wave (PAW) method, as implemented in the Vienna Ab initio Simulation Package (VASP).[26,27] The valence states included Sn [4d5s5p] and Se [4s4p] states. The structure optimization calculations employed the generalized gradient approximation (GGA) Perdew–Burke–Ernzerhof (PBE) functional[28] with a plane wave cutoff energy of 350 eV and a Γ-centered *k*-spacing of 0.2 $Å^{-1}$.

3. RESULTS & DISCUSSION

3.1. Crystal structures. Table 1 summarizes the crystal structure characteristics and chemical compositions of the SnSe films grown on glass and MgO (001) substrates. Detailed information of crystal structure and chemical composition analyses are summarized in **Figs. S2−S9** of Supporting Information. The *a*-axis oriented SnSe polycrystalline films were grown on glass substrates at T_g = RT−500 °C (**Fig. S2** of Supporting Information). The Se/Sn ratio was almost constant at 1.00−1.01, regardless of T_g. With increase of T_g, the *a*-axis lattice parameter (*a*) decreased and the *c*-axis one (*c*) increased, while the *b*-axis one (*b*) was almost constant. As seen in **Fig. 1**, Se−Sn−Se chemical bonding is formed along the *b*-axis while non-bonding Sn−Se connects along the *a*- and *c*-axes; that is, the non-bonding states are more fragile and easily deformed by temperature variation. As a result, the lattice volume (*V*) increased and became close to that (212.29 $Å^3$) of SnSe bulk[29] at higher T_g. FWHM values of out-of-plane 400 diffraction peaks ($\Delta\omega_{400}$) decreased from 10.5° to 4.8° with increase of T_g up to 500 °C; i.e., the degree of *a*-axis orientation was significantly improved by increasing T_g. The in-plane Scherrer crystallite sizes (*D*) increased from ~8 to ~20 nm with increase of T_g. The *a*-axis oriented SnSe film was epitaxially grown on the MgO (001) substrate with 90° rotational in-plane domain structure, i.e., the epitaxial relationship was [100] SnSe || [001] MgO for out-of-plane direction and [010][001]SnSe || MgO [100] for in-plane direction. The *c* was slightly

smaller and the a was larger than those of the film grown on glass substrate at same T_g = 500 °C. It is considered that the in-plane compressive strain −3.7% along the c-axis from the MgO substrate (a = 4.210 Å) decreased the c of the film, while the expansion of a was caused by the epitaxial strain.[8] The $\Delta\omega_{400}$ was 0.2°, indicating the strong a-axis orientation along out-of-plane direction. The SnSe epitaxial film exhibited the spiral domain growth (**Fig. S6** of Supporting Information), and the in-plane Scherrer D was estimated to be ~17 nm.

Figure 2 compares the plan-view STEM images for the a-axis oriented SnSe polycrystalline film grown on glass substrate and the epitaxial film grown on MgO (001) substrate at the same T_g = 500 °C. For the SnSe film on glass substrate (**Fig. 2(a)**), 100–200 nm sized granular structures were observed. The electron diffraction showed the ring pattern (inset of **Fig. 2(a)**), indicating that the SnSe films formed randomly oriented domain structures along the in-plane direction. On the other hand, a unique GB structure was found for the SnSe epitaxial film on MgO substrate (**Fig. 2(b)**). The lattice images of SnSe in A and B domains, rotated by 90°, were clearly observed, but the boundary between A and B domains was formed along the [011] and [01-1] directions, as indicated by the yellow line. In the crystal structure of layered SnSe, the adjacent layer is shifted by [0, 0, 0.38] along the c-axis, as indicated by the arrow in the right panel of **Fig. 1**. It was thought that two simple 90° rotational coincident GB structures could exist. One is built directly by the connection of a [010] oriented domain to a [001] oriented domain (**Fig. 1**). However, in this structure, the top SnSe molecular layer can form Sn−Se bonds but the second SnSe molecular layer would form Sn−Sn and Se−Se bonds; therefore, we can speculate this GB structure would be energetically / chemically unstable. On the other hand, as will be discussed later with **Fig. 7(a)**, a GB structure where a [011] oriented domain connected to a [01-1] oriented domain forms Sn−Se bonds in all the layers and is expected to be stabler. This structure is actually observed by STEM in **Fig. 2(b)**.

3.2. Electron transport properties. Figure 3 compares the temperature (T) dependences of

electronic properties for the *a*-axis oriented SnSe polycrystalline films on glass substrates and the epitaxial film on MgO (001) substrate. Here, Hall effect measurements and analyses were conducted by selecting samples with the significantly different conditions of low T_g (RT, 100°C) and high T_g (400°C, 500°C). All the films showed the decreasing σ with decreasing T, being semiconducting behaviors (**Fig. 3(a)**). The SnSe polycrystalline films on glass substrates exhibited $\sigma = 0.1$ S/cm at 300 K, regardless of different T_g. The σ was almost the same with the epitaxial film on MgO substrate. All films showed positive R_H, substantiating p-type conduction. The n of holes decreased with decrease of T (**Fig. 3(b)**). The n at 300 K for SnSe polycrystalline films on glass substrates gradually decreased from 10^{17} cm^{-3} to 10^{16} cm^{-3} with increasing T_g from RT to 500 °C. It is well known that the Sn vacancy (V_{Sn}) acts as a shallow acceptor in SnSe.[30,31] We could not detect any difference in the Sn/Se chemical compositions (**Table 1**); however, the increase of n is speculated to originate from the increase in the amount of V_{Sn} as T_g decreases. Detailed discussion is described in Supporting Information (**Figs. S10–S12**). The μ of all the films decreased with decreasing T due to the strong carrier scattering at lower T. On the other hand, μ at 300 K varied significantly with the change of T_g. The μ was 5 cm^2/(Vs) at 300 K for SnSe films grown at RT, and it increased to 46 cm^2/(Vs) as T_g increased to 500 °C. On the other hand, the SnSe epitaxial film showed comparable $\mu = 49$ cm^2/(Vs) at 300 K and a similar T dependence to those for the SnSe films grown on glass substrate at 500 °C, despite the large difference in the in-plane domain orientations.

3.3. Carrier mobility analysis. The T dependence of μ in the Arrhenius plots (**Fig. 4(a)**) showed thermally activated behaviors. For all the films, the $\ln(\mu T^{1/2})$ vs T^{-1} plots exhibited negative-sloping straight lines in the whole T range, suggesting that the hole transport in these films was dominated by GB scattering, as proposed by Seto,[32] with the form of $\ln\left(\mu T^{1/2}\right) = -\frac{E_b}{k_B T} + \ln\left(\frac{Lq}{\sqrt{2\pi m^* k_B}}\right)$, where E_b is the GB potential barrier height, L domain size, m^* the carrier

effective mass, k_B Boltzmann constant, q elementary charge. In this case, hole transport is disturbed by potential barriers formed due to the holes trapped by donor-type defects at the GBs. The E_b and L were estimated by fitting the Seto model to the experimental results, as shown by solid lines in **Fig. 4(a)**. The E_b decreased from 62 meV to 30 meV with increasing T_g from RT to 500 °C (top panel of **Fig. 4(b)**). By the Seto model, E_b in many semiconductors tend to decrease with increasing n, because higher-density carriers screen the GB background charges and reduce the GB barrier height. However, the E_b of SnSe polycrystalline films on glass substrates showed an opposite trend; i.e., E_b decreased with decreasing n. This result suggests that the improved a-axis orientation of SnSe polycrystalline films leads to low hole trap density and the reduction of E_b at the GBs with increasing T_g, as will be discussed later. Then, L was estimated using reported m^* values of 0.16 m_0 along the c-axis and 0.38 m_0 along the b-axis.[33] The L values averaged along the b- and c-axes are plotted in the middle panel of **Fig. 4(b)**. L increased from 3 to 8 nm, which is almost consistent with the Scherrer D from XRD measurements (**Table 1**). We calculated the mean free path of hole using the thermal velocity ($v = \sqrt{3k_B T/m^*}$) (note the films are non-degenerated) and carrier life time (τ) estimated from the Hall mobility and the band effective mass ($\tau = \mu m^*/e$). The mean free path of hole is estimated to be 1.69 nm for SnSe epitaxial film with μ = 49 cm^2/(Vs) at T = 300 K. This value is smaller than the Scherrer radius, indicating the intra-grain scattering such as phonon scattering dominates and reduces the mean free path. Then, we estimated in-grain carrier mobility (μ_g) by extrapolating E_b to 0, leading to the formula $\mu_g = \left(\frac{Lq}{\sqrt{2\pi m^* k_B}}\right) T^{-1/2}$. The μ_g at T = 300 K increased from 58 to 157 cm^2/(Vs) with increase of T_g (bottom panel of **Fig. 4(b)**), which related to the increase of grain size, the improvement of the crystal quality, and the decrease of V_{Sn} defects at higher T_g. The SnSe epitaxial film exhibited almost the same GB properties (E_b = 30 meV, L = 9 nm) as the polycrystalline film grown on glass substrate at the same T_g = 500 °C. The μ_g = 186 cm^2/(Vs) is comparable to μ = 240 cm^2/(Vs) along the b-axis

and 130 $cm^2/(Vs)$ along the c-axis of the SnSe single crystal.[1] Therefore, each crystallite in the SnSe films grown both on MgO (001) and glass substrates at T_g = 500 °C exhibited single-crystal-like electron transport properties, but the GB potential barrier is the limiting factor of carrier transport.

Based on the Seto model, the hole trap state density (Q_t) at the GBs was characterized by the equation of $Q_t = -\sqrt{\frac{8E_b\varepsilon n_A}{q}}$, where the ε is the dielectric permittivity and the n_A is acceptor state density. The n_A was estimated from the Arrhenius plots of n (**Fig. S10(c)** of Supporting Information), and the Q_t was calculated by using the reported ε values ~62 along the b-axis and ~42 along the c-axis.[34] The Q_t values averaged along the b- and c-axes are plotted in **Fig. 5(a)**. The Q_t of all the films were smaller than the total number of the acceptors in a grain (Ln_A), suggesting that only the region near the GBs was depleted while free holes remain in the other regions. The Q_t of SnSe films on glass substrates decreased from 4.9×10^{13} cm^{-2} to 2.0×10^{13} cm^{-2} as T_g increased from RT to 500 °C. On the other hand, the SnSe epitaxial film on MgO (001) substrate showed much smaller $Q_t = 1.3\times10^{13}$ cm^{-2}. The variation of E_b and Q_t in the SnSe films at low and high T_g is illustrated in **Fig. 5(b)**. The grain size of the SnSe films increases at higher T_g condition, resulting in the decrease of GB density. The Ln_A value was almost unchanged with the change of T_g, while the Q_t decreased, resulting in the lower E_b and higher μ for SnSe films grown at higher T_g.

3.4. Origin of carrier scattering in SnSe films. Here, we summarize the relationship between μ, crystallite orientations, and GB characteristics for SnSe films. The μ for a-axis oriented SnSe polycrystalline films increases as the out-of-plane $\Delta\omega_{400}$ decreases with increasing T_g, indicating that the a-axis orientation of the SnSe layers affects the carrier transport significantly (**Fig. 6(a)**). At the same time, the decrease of $\Delta\omega_{400}$ results in a decrease of E_b, which also leads to an increase in μ (**Figs. 6(b)**). On the other hand, the μ and E_b hardly change when $\Delta\omega_{400}$

becomes below 5°. Based on these findings, it can be concluded that the GBs of SnSe films with poor a-axis orientation form higher E_b, significantly reducing the μ. On the other hand, if the SnSe layers are strongly oriented along the a-axis with $\Delta\omega_{400} \leq 5^o$, the impact of a-axis orientation fluctuations on μ becomes small. The SnSe epitaxial film with much smaller $\Delta\omega_{400}$ = 0.2° exhibits almost the same μ ~ 50 cm^2/(Vs) for the SnSe polycrystalline films grown at T_g = 500 °C, regardless of the large difference in the in-plane domain orientations. This result suggests that the GBs formed by 90° rotational domain structure are the limiting factor of μ in the SnSe films with $\Delta\omega_{400} \leq 5^o$. Note that the FWHM of rocking curves represents not only misorientations of the crystallites but also other factors such as dislocations and lattice strain. Further analysis by atomic-scale characterization is necessary to separately address the effect of dislocations, misorientations, and lattice strain on the carrier mobility of SnSe films. We have previously reported the electronic properties of SnSe films on MgO (001) substrates with different T_g = 300–500 °C.[8] Epitaxial growth of SnSe film was confirmed at T_g = 400-500 °C, but the out-of-plane a-axis oriented films with no in-plane orientation was obtained at T_g = 300 °C. The μ of SnSe epitaxial films at RT slightly decreased from 49 cm^2/(Vs) for T_g = 500 °C to 41 cm^2/(Vs) for T_g = 400 °C. The low T_g growth decreases the grain size and reduces in-grain mobility. The $\Delta\omega_{400}$ increased from 0.2° for T_g = 500 °C to 0.5–0.7° for T_g = 400 °C. The SnSe epitaxial film for T_g = 400 °C shows higher a-axis orientation and higher μ than 20 cm^2/(Vs) for the a-axis oriented film on glass substrate at the same T_g. The grain size and a-axis orientation should be dominant factor for in-grain carrier mobility, but the μ also limited by GB scattering.

We then evaluated the electronic structures of SnSe with 90° rotational domains by density functional theory calculations. As discussed in section 3.1, the SnSe epitaxial film on MgO (001) substrate formed a boundary with a [011] oriented and a [01-1] oriented domains. We built a SnSe GB model based on the experimental observations as follows. First the primitive SnSe cell was fully relaxed including the lattice parameters and the atomic positions. Then a

1×2×2 supercell was generated based on the relaxed structure. The SnSe domain was created by cutting the supercell with the (011) surface, followed by a 90° rotation to create another SnSe domain. These two domains were connected by the (011) surface to form the final SnSe GB model.

Figures 7(a,b) show the plan view and cross-sectional view of the SnSe GB model with the boundary between the [011]-oriented A domains and the [01-1]-oriented B domains (indicated by blue dashed lines). The A and B domains are connected through the $Sn{-}Se_3$ polyhedra at the boundary in 1st and 2nd SnSe layers. **Figure 7(c)** shows the electronic band structure of SnSe GB model with the domain boundary. The in-gap state (red colored band) is found above the fundamental VBM of ideal SnSe (black bands). **Figures 7(a,b)** map the charge density at the VBM (indicated by arrow in **Fig. 7(c)**), which primarily concentrates in the vicinity of the domain boundary. A shift of SnSe molecular layers is observed between the A and B domains (arrows in **Fig. 7(a)**), and the domain boundary structure shows a distortion of chemical bonds; i.e., the in-plane Sn−Se bond lengths (2.76−2.95 Å) differ from those in the bulk SnSe model (2.82 Å), and the in-plane Sn−Sn distance (4.06−4.62 Å along *b*-axis and 4.07−4.89 Å along *c*-axis) are more diverse compared to the bulk SnSe model (4.20 Å along *b*-axis and 4.56 Å along *c*-axis). This distortion originates from the strain induced by the connection of the [011] and the [01-1] oriented SnSe domains that have different in-boundary *b*-axis length (4.20 Å) and *c*-axis length (4.56 Å). From the partial density of states (DOSs) of the SnSe GB model (**Fig. 7(d)**), Sn 5s, 5p and Se 5p form the VBM. Therefore, the distortion increases the Sn(5s,5p)−Se(5p) hybridization, causing the holes to become localized within the $Sn{-}Se_3$ polyhedra, which contributes to the hole trapping state with large E_b and restricts the μ of SnSe films.

4. CONCLUSIONS

We investigated the origin of carrier scattering through nanoscale characterization of *a*-axis oriented SnSe films with different *a*-axis misorientations and rotational GBs. The *a*-axis oriented SnSe polycrystalline films grown on glass substrates and epitaxial films on MgO (001) substrates showed p-type conduction, and the hole transport in the films was dominated by GB scattering. GBs of SnSe films with low *a*-axis orientation ($\Delta\omega_{400} \geq 5°$) formed high GB potential barriers with E_b up to 60 meV and significantly reduced the μ. The μ at 300 K for SnSe polycrystalline films on glass substrates was 5 cm^2/(Vs) at RT, but increased to 46 cm^2/(Vs) due to the increased grain size and improved $\Delta\omega_{400}$ as the T_g increased to 500 °C. Meanwhile, when $\Delta\omega_{400}$ of the SnSe layers was decreased to < 5°, the impact of *a*-axis orientation fluctuations on μ became small. It was found that SnSe epitaxial films with 90° rotational domain structure formed the domain boundary between the [011] oriented and the [01-1] oriented domains. The 90° rotational domain boundary caused a shift of SnSe molecular layers between the [011] and [01-1] oriented grains and the distorted Sn–Se_3 polyhedra formed hole trap states with E_b = 30 meV, limiting the maximum μ ~50 cm^2/(Vs) of SnSe films. We also believe that similar GB structures widely present in polycrystalline films, which should be further investigated in future work. It should be noted that the orthorhombic SnSe can be considered distorted from the cubic structure.[24] While the orthorhombic one employs covalent bonding, the cubic one utilizes metavalent bonding.[35] The degree of structural distortions affects the bonding mechanism and thus the transport properties through the GBs by changing the T_g, but further structure analyses are necessary for the discussion. These findings would be beneficial for understanding the carrier transport properties of SnSe films and the control of crystallite orientation and size is important to further enhance the carrier mobility and thermoelectric properties for device applications. The crystallite orientation can be improved and the crystallite size can be enlarged by increasing the T_g. However, the maximum T_g is limited by severe re-evaporation of the films at ≥ 600 °C in a vacuum. Therefore, it is considered difficult to improve the mobility by changing the T_g during the deposition. On the other hand, post-heat treatment at higher

temperature, while suppressing the volatilization, should be effective in further improving the crystal quality and enlarging the grain size. For example, preparing a surface capping layer to suppress the volatilization, followed by post-annealing in Ar atmosphere, or performing rapid laser annealing, could be more effective. It also should be noted that the poor performance of polycrystalline SnSe bulk is attributed to the formation of tin oxides covering the surface of SnSe powders, which increases thermal conductivity, reduces electronic conductivity and thereby reduces ZT.[36] It should be important to investigate nanoscale chemical composition analysis near the GBs and the effect of heat treatment under reducing conditions on the electronic properties through rotational GBs in the SnSe films.

Finally, it should be noted that the deterioration of μ by GBs is also observed in tin mono-sulfide (SnS),[37,38] a potential semiconductor for solar cells, and tin monoxide (SnO),[39,40] a potential wide-gap p-type semiconductor. They have similar layered crystal structures, and there may be a similar mechanism limiting the μ at the GBs. Further investigation is expected in the epitaxial films to improve their semiconductor device properties.

ASSOCIATE CONTENT

Supporting Information

Supporting Information is available free of charge.

Supporting information for growth and carrier transport analyses of SnSe films on glass and MgO (001) substrates.

AUTHOR INFORMATION

Corresponding Authors

Takayoshi Katase; katase.t.aa@m.titech.ac.jp

Toshio Kamiya; kamiya.t.aa@m.titech.ac.jp

Author contributions

X.H., K.M., K.H., H.Y. contributed to the thin film fabrication and characterization. All authors discussed the results and commented on the study. X.H., Ta.K., and To.K. co-wrote the manuscript. Ta.K. and To.K. proposed the idea and supervised the entire project.

Note

The authors declare no conflict of interest.

ACKNOWLEDGMENT

This work was supported by a project of Kanagawa Institute of Industrial Science and Technology (KISTEC). Part of this research was also supported by MEXT Program: Data Creation and Utilization Type Material Research and Development Project (Grant No. JPMXP1122683430), as well as by Design and Engineering by Joint Inverse Innovation for Materials Architecture, MEXT. Ta.K. was supported by Japan Society for the Promotion of Science (JSPS) through Grants-in-Aid for Scientific Research (B) (Grant No. JP23K23034), Scientific Research (S) (Grant No. JP22H04964), and Challenging Research (Exploratory) (Grant No. JP24K21671). H.Hi. was supported by JSPS through Grants-in-Aid for Scientific Research (A) (Grant Nos. JP20H00302, JP21H04612, and JP24H00376). The numerical calculations were carried out on the TSUBAME3.0 supercomputer at Tokyo Institute of Technology supported by the MEXT Project of the Tokyo Tech Academy for Convergence of Materials and Informatics (TAC-MI). A part of the present experiments was carried out by using a facility in the Comprehensive Analysis Center, SANKEN, Osaka University. The HAXPES experiments at SPring-8 were performed with the approval of NIMS Synchrotron X-ray Station (Proposal Nos. 2018A4701). The crystal structures in Figs. 1, 2(b), 7(a,b), S4(b), S7, and S12(a) were drawn using the VESTA code.[41]

References

(1) Zhao, L.-D.; Lo, S.-H.; Zhang, Y.; Sun, H.; Tan, G.; Uher, C.; Wolverton, C.; Dravid, V. P.; Kanatzidis, M. G. Ultralow thermal conductivity and high thermoelectric figure of merit in SnSe crystals. *Nature* **2014**, *508*, 373−377.

(2) Parenteau, M.; Carlone, C. Influence of temperature and pressure on the electronic transitions in SnS and SnSe semiconductors. *Phys. Rev. B* **1990**, *41*, 5227.

(3) Patel, T. H.; Vaidya, R.; Patel, S. G. Growth and transport properties of tin monosulphoselenide single crystals. *J. Cryst. Growth* **2003**, *253*, 52−58.

(4) Abrikosov, N. K.; Bankina, V. F.; Poretskaya, L. V.; Shelimova, L. E.; Skudnova, E. V. *Semiconducting II-VI, IV-VI, and V-VI Compounds*, Plenum Press, New York, **1969**, 110.

(5) Maier, H.; Daniel, D. R. SnSe single crystals: Sublimation growth, deviation from stoichiometry and electrical properties. *J. Electron. Mater.* **1977**, *6*, 693−704.

(6) Agarwal, A. Synthesis of laminar SnSe crystals by a chemical vapour transport technique. *J. Cryst. Growth* **1998**, *183*, 347−351.

(7) Nariya, B. B.; Dasadia, A. K.; Bhayani, M. K.; Patel, A. J.; Jani, A. R. Electrical transport properties of SnS and SnSe single crystals grown by direct vapour transport technique. *Chalcogenide Lett.* **2009**, *6*, 549−554.

(8) Inoue, T.; Hiramatsu, H.; Hosono, H.; Kamiya, T. Heteroepitaxial growth of SnSe films by pulsed laser deposition using Se-rich targets. *J. Appl. Phys.* **2015**, *118*, 205302.

(9) Jeong, G.; Kim, J.; Gunawan, O.; Pae, S. R.; Kim, S. H.; Song, J. Y.; Lee, Y. S.; Shin, B. Preparation of single-phase SnSe thin-films and modification of electrical properties via stoichiometry control for photovoltaic application. *J. Alloy Compd.* **2017**, *722*, 474−481.

(10) Gong, X.; Feng, M.; Wu, H.; Zhou, H.; Suen, C.; Zou, H.; Guo, L.; Zhou, K.; Chen, S.; Dai, J.; Wang, G.; Zhou, X. Highly (*100*)-orientated SnSe thin films deposited by pulsed-laser deposition. *Appl. Surface Sci.* **2021**, *535*, 147694.

(11) Heo, S.H.; Jo, S.; Kim, H.S.; Choi, G.; Song, J.Y.; Kang, J.Y.; Park, N.J.; Ban, H.W.; Kim,

F.; Jeong, H.; Jung, J.; Jang, J.; Lee, W.B.; Shin, H.; Son, J.S. Composition change-driven texturing and doping in solution-processed SnSe thermoelectric thin films. *Nat. Commun.* **2019**, *10*, 864.

(12) Horide, T.; Nakamura, K.; Ishimaru, M. Carrier Control of Bi-Doped SnSe Films for Fabrication of π-Type Thermoelectric Film Modules. *ACS Appl. Energy Mater.* **2024**, *7*, 346.

(13) Suen, C.H.; Shi, D.L.; Su, Y.; Zhang, Z.; Chan, C.H.; Tang, X.D.; Li, Y.; Lam, K.H.; Chen, X.X.; Huang, B.L.; Zhou, X.Y.; Dai, J.Y. Enhanced thermoelectric properties of SnSe thin films grown by pulsed laser glancing-angle deposition. *J. Materiomics* **2017**, *3*, 293–298.

(14) Horide, T.; Murakami, Y.; Hirayama, Y.; Ishimaru, M.; Matsumoto, K. Thermoelectric Property in Orthorhombic-Domained SnSe Film. *ACS Appl. Mater. Interfaces* **2019**, *11*, 27057−27063.

(15) Song, L.R.; Zhang, J.W.; Iversen, B.B. Enhanced thermoelectric properties of SnSe thin films grown by single-target magnetron sputtering. *J. Mater. Chem. A* **2019**, *7*, 17981–17986.

(16) Liu, S.Y.; Lan, M.D.; Li, G.J.; Yuan, Y.; Jia, B.H.; Wang, Q. Co dopant drives surface smooth and improves power factor of evaporated SnSe films. *Ceram. Int.* **2020**, *46*, 16578–16582.

(17) Li, Y. F.; Tang, G. H.; Nie, Y. N.; Zhang, M.; Zhao, X.; Shiomi, J. Synergetic optimization of thermoelectric properties in SnSe film via manipulating Se vacancies. *J. Alloy Compd.* **2023**, *943*, 169115.

(18) Burton, M.R.; Liu, T.; McGettrick, J.; Mehraban, S.; Baker, J.; Pockett, A.; Watson, T.; Fenwick, O.; Carnie, M.J. Thin film tin selenide (SnSe) thermoelectric generators exhibiting ultralow thermal conductivity. *Adv. Mater.* **2018**, *30*, 1801357.

(19) Okazaki, A.; Ueda, I. The Crystal Structure of Stannous Selenide SnSe. *J. Phys. Soc. Jpn.* **1956**, *11*, 470.

(20) Kutorasinski, K.; Wiendlocha, B.; Kaprzyk, S.; Tobola, J. Electronic structure and thermoelectric properties of n- and p-type SnSe from first-principles calculations. *Phys. Rev. B*

2015, *91*, 205201.

(21) Yang, S.; Liu, Y.; Wu, M.; Zhao, L.-D.; Lin, Z.; Cheng, H.; Wang, Y.; Jiang, C.; Wei, S.-H.; Huang, L.; Huang, Y.; Duan, X. Highly-anisotropic optical and electrical properties in layered SnSe. *Nano Res.* **2018**, *11*, 554–564.

(22) Mataré, H. F. Carrier transport at grain boundaries in semiconductors. *J. Appl. Phys.* **1984**, *56*, 2605–2631.

(23) Wu, R.; Yu, Y.; Jia, S.; Zhou, C.; Cojocaru-Mirédin, O.; Wuttig, M. Strong charge carrier scattering at grain boundaries of PbTe caused by the collapse of metavalent bonding. Nat. Commun. **2023**, *14*, 719.

(24) Katase, T.; Takahashi, Y.; He, X.; Tadano, T.; Ide, K.; Yoshida, H.; Kawachi, S.; Yamaura, J.; Sasase, M.; Hiramatsu, H.; Hosono, H.; Kamiya, T. Reversible 3D-2D structural phase transition and giant electronic modulation in nonequilibrium alloy semiconductor, lead-tin-selenide. *Sci. Adv.* **2021**, *7*, eabf2725.

(25) He, X.; Chen, J.; Katase, T.; Minohara, M.; Ide, K.; Hiramatsu, H.; Kumigashira, H.; Hosono, H.; Kamiya, T. High-Mobility Metastable Rock-Salt Type (Sn,Ca)Se Thin Film Stabilized by Direct Epitaxial Growth on a YSZ (111) Single-Crystal Substrate. *ACS Appl. Mater. Interfaces* **2022**, *14*, 18682−18689.

(26) Kresse, G.; Joubert, D. From ultrasoft pseudopotentials to the projector augmented-wave method. *Phys. Rev. B* **1999**, *59*, 1758−1775.

(27) Kresse, G.; Furthmüller, J. Efficient iterative schemes for ab initio total-energy calculations using a plane-wave basis set. *Phys. Rev. B* **1996**, *54*, 11169−11186.

(28) Perdew, J. P.; Burke, K.; Ernzerhof, M. Generalized gradient approximation made simple. *Phys. Rev. Lett.* **1996**, *77*, 3865–3868.

(29) Wu, P.; Ishikawa, Y.; Hagihala, M.; Lee, S.; Peng, K.; Wang, G.; Torii, S.; Kamiyama, T. Crystal structure of high-performance thermoelectric materials by high resolution neutron powder diffraction. *Physica B: Condens. Mater.* **2018**, *551*, 64–68.

(30) Huang, Y.; Wang, C.; Chen, X.; Zhou, D.; Du, J.; Wang, S.; Ning, L. First-principles study on intrinsic defects of SnSe. *RSC Adv.* **2017**, *7*, 27612.

(31) He, X.; Zhang, H.; Nose, T.; Katase, T.; Tadano, T.; Ide, K.; Ueda, S.; Hiramatsu, H.; Hosono, H.; Kamiya, T. Degenerated Hole Doping and Ultra-Low Lattice Thermal Conductivity in Polycrystalline SnSe by Nonequilibrium Isovalent Te Substitution, *Adv. Sci.* **2022**, *9*, 202105958.

(32) Seto, J. Y. W. The electrical properties of polycrystalline silicon films. *J. Appl. Phys.* **1975**, *46*, 5247−5254.

(33) Nagayama, T.; Terashima, K.; Wakita, T.; Fujiwara, H.; Fukura, T.; Yano, Y.; Ono, K.; Kumigashira, H.; Ogiso, O.; Yamashita, A.; Takano, Y.; Mori, H.; Usui, H.; Ochi, M.; Kuroki, K.; Muraoka, Y.; Yokoya, T. Direct observation of double valence-band extrema and anisotropic effective masses of the thermoelectric material SnSe. *Jpn. J. Appl. Phys.* **2017**, *57*, 010301.

(34) Chandrasekhar, H.; Humphreys, R. G.; Zwick, U.; Cardona, M. Infrared and Raman spectra of the IV-VI compounds SnS and SnSe. *Phys. Rev. B* **1977**, *15*, 2177.

(35) Lin, N.; Han, S.; Ghosh, T.; Schön, C.-F.; Kim, D.; Frank, J.; Hoff, F.; Schmidt, T.; Ying, P.; Zhu, Y.; Häser, M.; Shen, M.; Liu, M.; Sui, J.; Cojocaru-Mirédin, O.; Zhou, C.; He, R.; Wuttig, M.; Yu, Y. Metavalent Bonding in Cubic SnSe Alloys Improves Thermoelectric Properties over a Broad Temperature Range. *Adv. Funct. Mater.* **2024**, *34*, 15652.

(36) Zhou, C.; Lee, Y. K.; Yu, Y.; Byun, S.; Luo, Z.-Z.; Lee, H.; Ge, B.; Lee, Y.-L.; Chen, X.; Lee, J. Y.; Cojocaru-Mirédin, O.; Chang, H.; Im, J.; Cho, S.-P.; Wuttig, M.; Dravid, V. P.; Kanatzidis, M. G.; Chung, I. Polycrystalline SnSe with a thermoelectric figure of merit greater than the single crystal. *Nat. Mater.* **2021**, *20*, 1378−1384.

(37) Ran, F.-Y.; Xiao, Z.; Hiramatsu, H.; Hosono, H.; Kamiya, T. Growth of high-quality SnS epitaxial films by H_2S flow pulsed laser deposition. *Appl. Phys. Lett.* **2014**, *104*, 072106.

(38) Ran, F.-Y.; Xiao, Z.; Hiramatsu, H.; Ide, K.; Hosono, H.; Kamiya, T. SnS thin films prepared by H_2S-free process and its p-type thin film transistor. *AIP Adv.* **2016**, *6*, 015112.

(39) Minohara, M.; Kikuchi, N.; Yoshida, Y.; Kumigashira, H.; Aiura, Y. Improvement of the hole mobility of SnO epitaxial films grown by pulsed laser deposition. *J. Mater. Chem. C* **2019**, *7*, 6332–6336.

(40) Yabuta, H.; Kaji, N.; Hayashi, R.; kumomi, H.; Nomura, K.; Kamiya, T.; Hirano, M.; Hosono, H. Sputtering formation of p-type SnO thin-film transistors on glass toward oxide complimentary circuits. *Appl. Phys. Lett.* **2010**, *97*, 072111.

(41) Momma, K.; Izumi, F. VESTA 3 for three-dimensional visualization of crystal, volumetric and morphology data. *J. Appl. Crystallogr.* **2011**, *44*, 1272–1276.

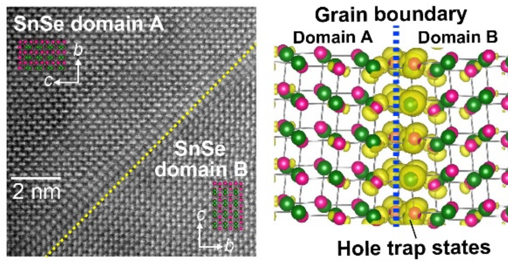

For Table of Contents Only

Table 1. Summary of lattice parameters, crystallite orientation, crystallite sizes, and chemical compositions of the *a*-axis oriented SnSe films grown on glass and MgO (001) substrates. T_g: growth temperature, *a*: *a*-axis lattice parameter, *b*: *b*-axis lattice parameter, *c*: *c*-axis lattice parameter, *V*: unit cell volume, $\Delta\omega_{400}$: full width at half maximum values of 400 diffraction peak, *D*: in-plane crystallite size estimated from Scherrer's equation using in-plane 020 and 002 diffractions.

Film form	Sub.	T_g (°C)	Sn/Se ratio	*a* (Å)	*b* (Å)	*c* (Å)	*V* (Å^3)	$\Delta\omega_{400}$ (°)	*D* (nm)
a-axis oriented film with in-plane randomly oriented domains	Glass	RT	1.01	11.649	4.179	4.261	207.43	10.5	7.99
		100	1.00	11.610	4.180	4.310	209.13	7.7	7.03
		400	1.00	11.513	4.179	4.404	211.88	5.8	18.41
		500	1.01	11.513	4.186	4.392	211.67	4.8	19.99
Epitaxial film with in-plane 90° rotational domains	MgO (001)	500	1.01	11.540	4.191	4.369	211.30	0.2	16.53

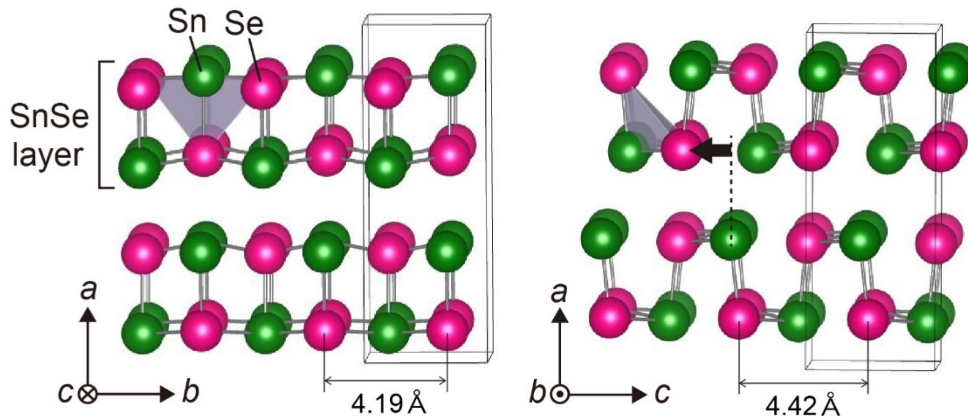

Figure 1. Crystal structure of *a*-axis oriented SnSe viewed from *c*-axis (left) and *b*-axis (right). SnSe has a layered crystal structure composed of alternately stacked SnSe layers along the *a*-axis. The 3-fold coordinated Sn–Se_3 unit of the SnSe layer is shown by the purple polyhedrons. SnSe has the largely different bonding network structures in plane along *b*-axis and *c*-axis.

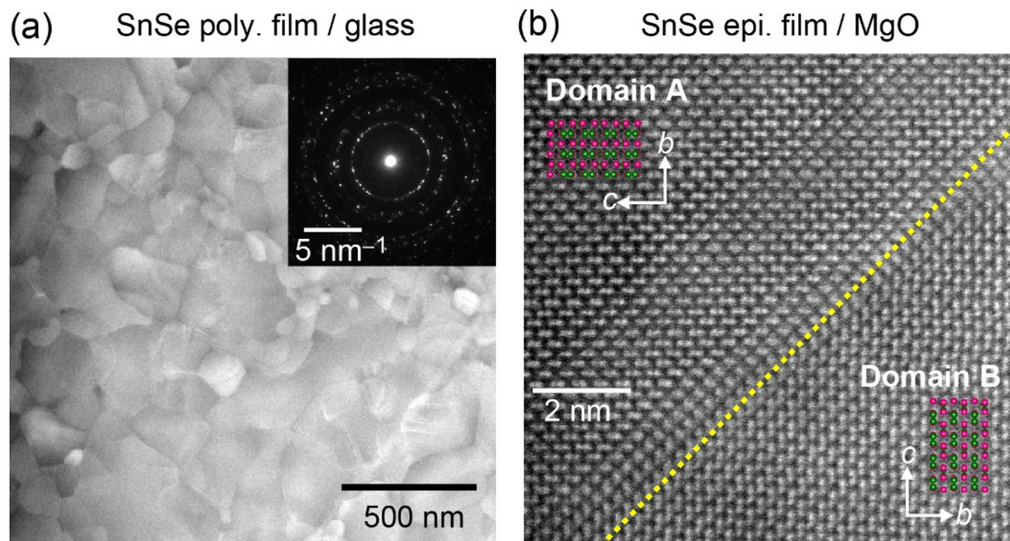

Figure 2. Plan-view STEM images of (a) *a*-axis oriented SnSe polycrystalline film grown on glass substrate at T_g = 500 °C and (b) SnSe epitaxial film grown on MgO (001) substrate at T_g = 500 °C. Electron diffraction pattern of SnSe polycrystalline film is shown in the inset of (a). The lattice illustrations of SnSe are superimposed in the inset of (b). Green and pink spheres indicate Sn and Se atoms, respectively.

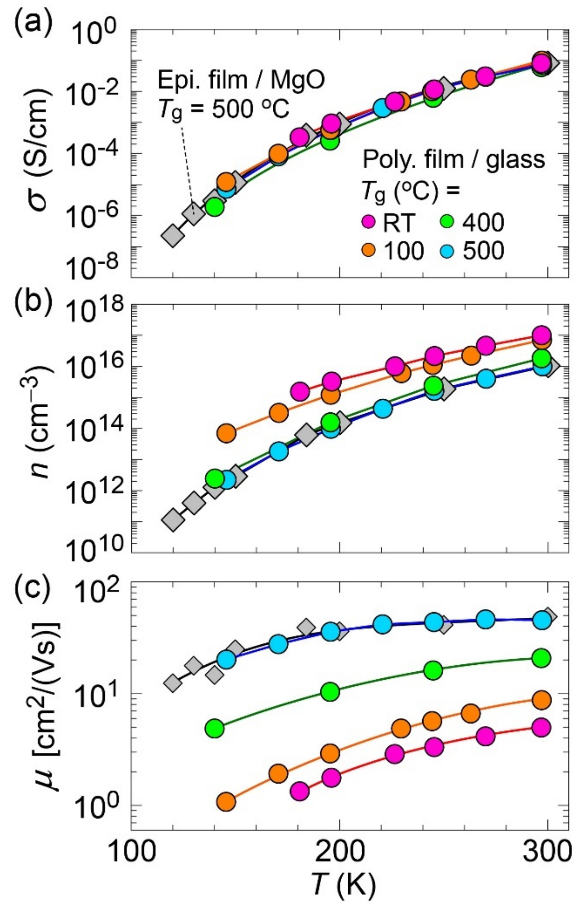

Figure 3. Temperature (*T*) dependences of electron transport properties for the *a*-axis oriented SnSe polycrystalline films on glass substrates and the epitaxial film on MgO (001) substrate. (a) Electrical conductivity (*σ*), (b) hole concentration (*n*), and (c) Hall mobility (*μ*).

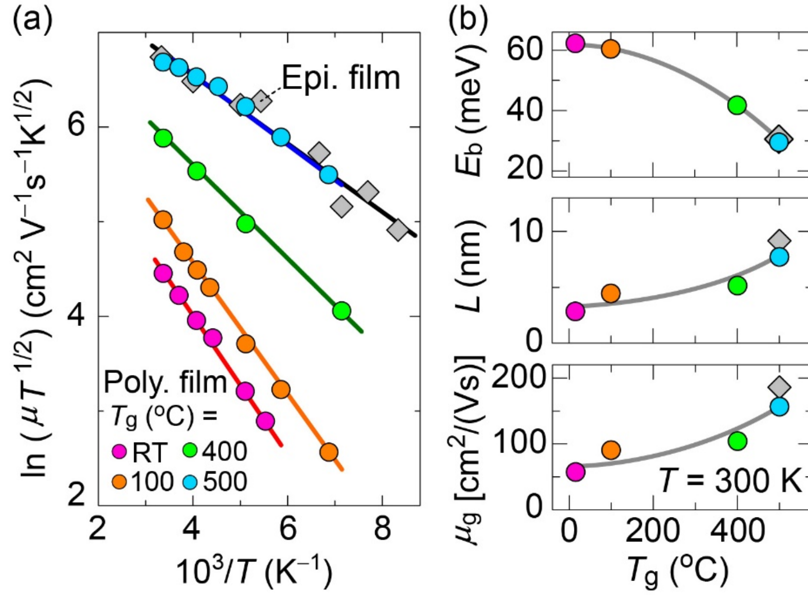

Figure 4. (a) Arrhenius plots of μ for SnSe films on glass and MgO (001) substrates. (b) Grain boundary potential barrier height (E_b), domain size (L), and in-grain carrier mobility (μ_g) at T = 300 K and E_b = 0 eV, estimated by fitting the Seto model to experimental results, as shown by solid lines in (a).

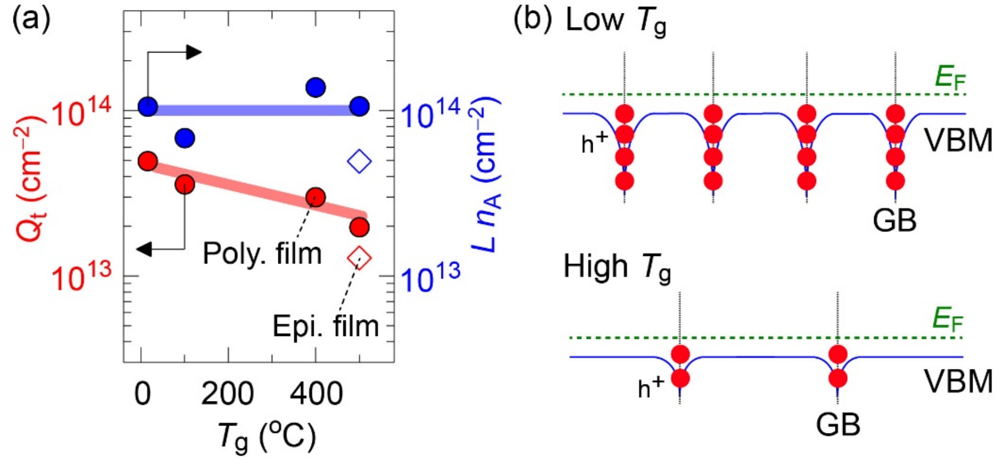

Figure 5. (a) T_g dependences of hole trap state density (Q_t) at GBs and the total number of acceptors in a grain (Ln_A) for SnSe polycrystalline films on glass substrates and the epitaxial film on MgO (001) substrate. (b) Energy diagram of the valence band maximum (VBM, blue lines) near the GBs for SnSe films with low T_g (upper image) and high T_g (bottom image). Green dotted lines indicate the E_F position. The trapped holes (h^+) are shown by red circles.

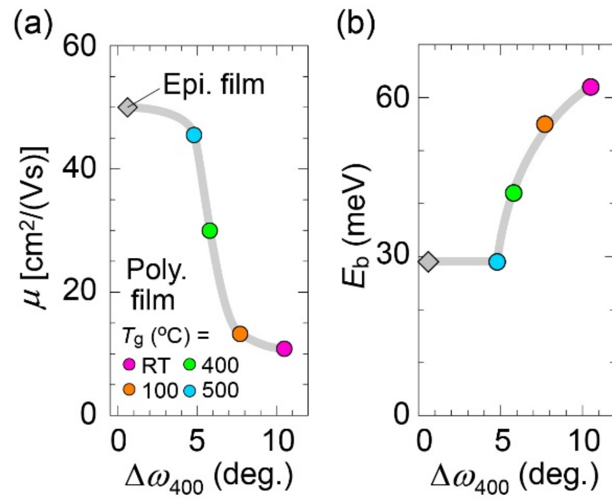

Figure 6. Relationship between μ, crystallite orientations, and GB characteristics for SnSe films at RT. (a) μ vs. FHWM values of out-of-plane 400 rocking curves ($\Delta\omega_{400}$). (b) GB potential barrier height (E_b) vs. $\Delta\omega_{400}$.

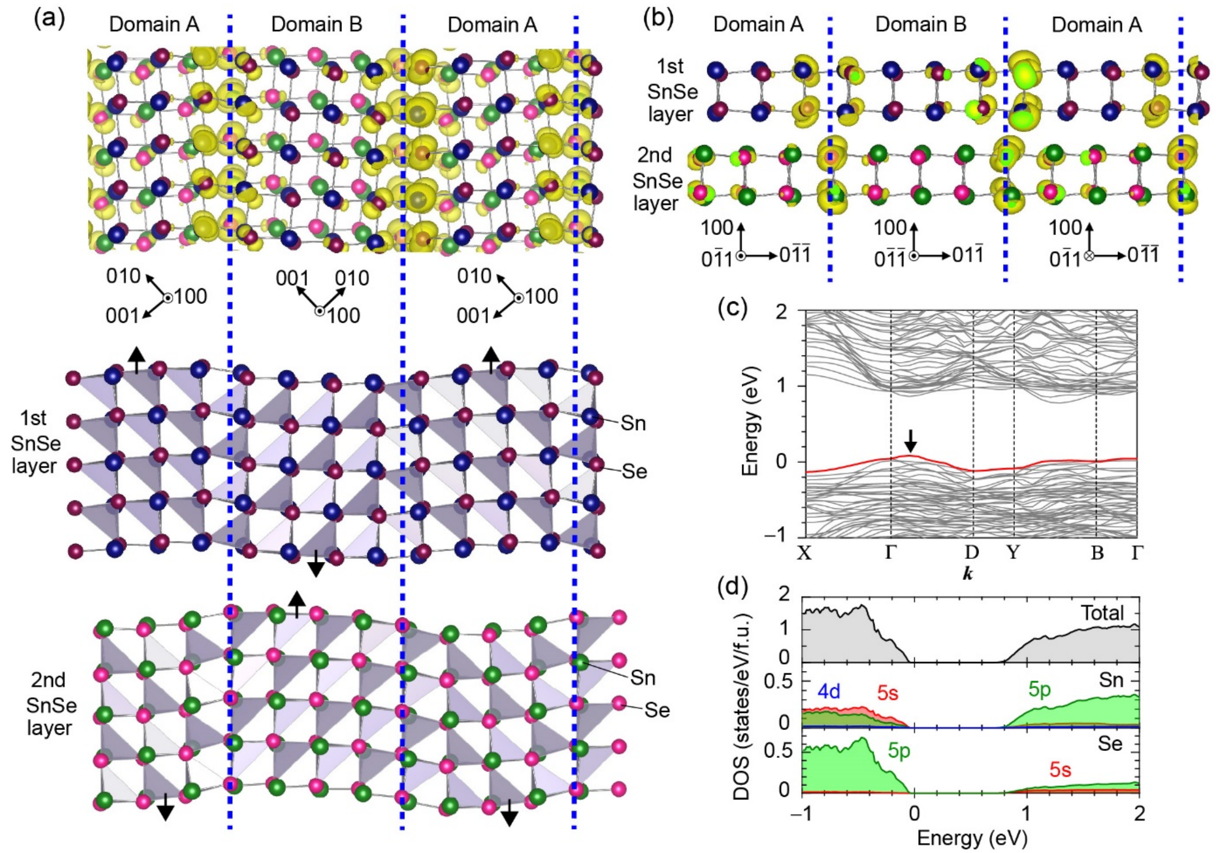

Figure 7. (a) Plan view of SnSe GB model with 90°-rotational A and B domains, where the boundary is formed along [110] and [01-1] direction, indicated by blue dotted lines. Charge density map at VBM is shown in the top image. The middle and bottom images show the Sn−Se_3 polyhedra in 1st and 2nd SnSe layers, respectively. (b) Cross-sectional view of the SnSe GB model and charge density map at VBM. (c) Electronic band structures along the *k*-path of X (0.5, 0, 0), Γ (0, 0, 0), D (0, -0.5, -0.5), Y (0, 0.5, 0), B (0, 0.5, -0.5), (d) partial DOSs of the SnSe model.